Journal of Materials Chemistry A

Accepted Manuscript

ROYAL SOCIETY OF CHEMISTRY

www.rsc.org/materialsA

Effect of Solvents on the Growth of TiO_2 Nanorods and Their Perovskite Solar Cells

Jun-Feng Li [a], Zhen-Long Zhang [a, *], Hui-Ping Gao [a], Yang Zhang [a], Yan-Li Mao [a, b, *]

[a] School of Physics and Electronics, Henan University, Kaifeng 475004, China

[b] Institute for Computational Materials Science, Henan University, Kaifeng 475004, China

*Corresponding author: +86-371-23893703; E-mail: zhenlong2015@163.com (Z.L. Zhang); ylmao1973@163.com (Y.L. Mao)

Abstract: TiO_2 nanorods were synthesized by the hydrothermal methods with ethanol-HCl and water-HCl solutions, respectively, and $CH_3NH_3PbI_{3-x}Cl_x$ perovskite solar cells based on them were fabricated. The power conversion efficiency (PCE) of the best solar cells based on TiO_2 nanorods with water-HCl solution is higher than that with ethanol-HCl solution. The dimension, morphology, optical property, and photogenerated charge behavior of the two kinds of samples were investigated. The results indicate that the better performance of solar cells based TiO_2 nanorods with water-HCl solution than that with ethanol-HCl solution could be attributed to its special orientation, high conductivity, improved morphology, good optical property, fast charge transfer and reduced charge recombination. The PCE of 11.8% was achieved using the TiO_2 nanorods with water-HCl solution, which is the highest in the reported TiO_2 nanorods based cells.

Introduction

Since the first report of $CH_3NH_3PbI_3$ based solid-state solar cells in 2012 [1], organic-inorganic hybrid perovskite solar cells have attracted considerable attention due to their special properties, such as large absorption coefficient, electron-hole diffusion length, and high charge carrier mobility [2-9]. The power conversion efficiency (PCE) of perovskite solar cells has been over 20% [10]. In general, perovskite solar cells are constructed with a perovskite layer sandwiched between a

electron transfer material (ETM) layer and a hole transfer material (HTM) layer. Mesoporous TiO_2 has been used as the ETM in most of the perovskite solar cells [11-14]. However, the main issue is the difficulty in pore filling for the mesoporous structure [15]. Compared with the mesoporous structure, one dimensional (1D) nanostructure has some advantages, such as easy pore filling of active layer or HTM, better electron transfer and lower charge recombination [16, 17].

Rutile TiO_2 nanorods (NRs) have been widely applied to perovskite solar cells [18-22]. Among the synthesis methods of TiO_2 NRs, hydrothermal synthesis has been usually adopted due to the low temperature and no requirement of expensive apparatus. For the hydrothermal synthesis of TiO_2 NRs, Ti precursors are dissolved in water-HCl solution in some reports [18-21], while in ethanol-HCl solution in others [22]. However, the effect of solvents (ethanol and water) on the growth of TiO_2 NRs and their perovskite solar cells performance are not clear.

Therefore in the present study, we synthesized TiO_2 NRs with the both methods. The dimension of TiO_2 NRs, including the length, diameter, and density, was controlled by adjusting the growth time. The $CH_3NH_3PbI_{3-x}Cl_x$ ($MAPbI_{3-x}Cl_x$) perovskite solar cells were fabricated using the TiO_2 NRs as an ETM layer. The characteristics of TiO_2 NRs and their perovskite solar cells performance were investigated. The effect of solvents on the growth of TiO_2 NRs and their perovskite solar cells performance was discussed. By optimizing the parameters, the high power conversion efficiency (PCE) of 11.8% was achieved for the perovskite solar cells based on TiO_2 nanorods with water-HCl solution.

Results and Discussion

Figure 1 shows the XRD patterns of TiO_2 NRs grown on FTO glass substrates, respectively. The diffraction peaks at 26.6^o, 38.0^o, and 51.6^o were assigned to (110), (200), and (211) planes of SnO_2 (JCPDS card, 41-1445) on FTO substrate, respectively. The diffraction peaks at 36.2^o and 62.8^o were assigned to the (101) and (002) plane of rutile TiO_2 (JCPDS, 21-1276), respectively [23], which indicates that the TiO_2 NRs films have (101) and (002) planes. The peak intensity ratio of (002) and

(101), $I_{(002)}/I_{(101)}$ is 89.1 for TiO_2 NRs (e), which suggests that crystallites grew preferentially with (002) plane parallel to the substrate surface. While only (101) peak appears in the XRD pattern of TiO_2 NRs (w), which indicates almost all the crystals grew with (101) plane parallel to the substrate surface [24].

The dimension of the TiO_2 NRs, such as the length, diameter, and density, was changed by adjusting the growth time in the autoclave. The $MAPbI_{3-x}Cl_x$ perovskite solar cells were fabricated using the as-made TiO_2 NRs. The relationship between the photovoltaic performance of solar cells and the growth time was investigated. Figure 2 shows the dependence of the power conversion efficiency (PCE) on the growth time. The PCE of solar cells increases firstly, and then decreases with the increasing of growth time, which reaches the maximum at the growth times of 60 min and 120 min for TiO_2 NRs (e) and TiO_2 NRs (w), respectively. The average PCEs of the solar cells based on TiO_2 NRs (e) and TiO_2 NRs (w) with the optimal growth times are 7.5% and 10.5%, respectively.

Figure 3 shows the J-V curves of the best solar cells based on TiO_2 NRs (e) and TiO_2 NRs (w). The short current (J_{sc}), open voltage (V_{oc}), fill factor (FF) and power conversion efficiency (PCE) were obtained from J-V curves averaged with reverse and forward bias sweep. The PCEs of best solar cells based on TiO_2 NRs (e) and TiO_2 NRs (w) are 8.6% and 11.8%, respectively. Morerover, the J_{sc}, V_{oc}, and FF of solar cells based on TiO_2 NRs (w) are larger than those on TiO_2 NRs (e). Figure 4 shows the IPCE of the perovskite solar cells based on TiO_2 NRs (w) and TiO_2 NRs (e). The integrated J_{sc} calculated from IPCE data are 18.9 and 21.0 mA/cm^2 for cells based on TiO_2 NRs (e) and TiO_2 NRs (w), respectively. The IPCE at the entire wavelength range and the calculated J_{sc} of the cells based on TiO_2 NRs (w) are larger than those on TiO_2 NRs (e), which agree with the J-V measurements.

XRD patterns shown in Figure 1 display that the TiO_2 NRs (e) and TiO_2 NRs (w) are highly ordered nanorods with (002) and (101) facets exposed on top, respectively. It was reported that the (101) facet of rutile TiO_2 is a more reactive facet than other facets due to its low energy vacancy formation energy [25]. The better performance of perovskite solar cells based on TiO_2 NRs (w) than that on TiO_2 NRs (e) could be due

to the reactive (101) facet.

To further get insights to this phenomenon, some investigations were performed. The series resistance (R_s) and shunt resistance (R_{sh}) were calculated from illuminated J-V curves converging to V_{oc} and J_{sc}, respectively. A reduced R_s of 5.80 Ωcm^2 of TiO_2 NRs (w) based cells was observed compared to TiO_2 NRs (e) based cells (8.65 Ωcm^2), implying a superior charge transport ability of TiO_2 NRs (w). Moreover, the shunt resistance (1.15 $k\Omega cm^2$) of TiO_2 NRs (w) based cells was larger than that of TiO_2 NRs (e) based cells (0.35 $k\Omega cm^2$), which indicates that carrier recombination could be more efficiently reduced for the cells based on TiO_2 NRs (w).

Figures 5a and c show the plane-view and cross sectional SEM images of TiO_2 NRs (e) films for 60 min growth, and Figures 5b and d show those of TiO_2 NRs (w) films for 120 min growth. The dimension of the TiO_2 NRs (e) was determined to be 53±8 nm wide and 1.9±0.1 μm long, and that of TiO_2 NRs (w) was determined to be 32±5 nm wide and 0.5±0.05 μm long. It indicates that the growth rate of TiO_2 NRs (e) is larger than that of TiO_2 NRs (w). The TiO_2 NRs (w) are homogeneous and vertically aligned on the substrate, while the TiO_2 NRs (e) displays a reduced degree of order and alignment. Figures 5e and f show the cross sectional SEM images of the best solar cells based on TiO_2 NRs (e) and TiO_2 NRs (w), respectively. The top Au electrode is separated from the photoanode. Pores of nanorods are filled by $MAPbI_{3-x}Cl_x$, on which a capping layer of perovskite was formed. The thickness of capping layer on TiO_2 NRs (w) is uniform in the view, while that on TiO_2 NRs (e) is inhomogeneous, which could be due to the different dimension of TiO_2 NRs films shown in Figures 5a and b. The Spiro-OMeTAD layer is well separated by the capping layer from nanorods films in the cells based on TiO_2 NRs (w), compared with that on TiO_2 NRs (e). The possibility of HTM layer to contact with TiO_2 NRs (w) film directly is smaller than that with TiO_2 NRs (e), which decreases the electron-hole recombination.

Figure 6A shows the XRD patterns of TiO_2 NRs (e)/$MAPbI_{3-x}Cl_x$ and TiO_2 NRs (w)/$MAPbI_{3-x}Cl_x$. The diffraction peaks at 14.2° and 28.6° are assigned to the (110) and (220) planes of $MAPbI_{3-x}Cl_x$, respectively [26]. There is no any difference in the

crystal structure of $MAPbI_{3-x}Cl_x$ layer grown on these two kinds of TiO_2 NRs. Figure 6B shows the UV-vis absorption spectra of TiO_2 NRs (e)/$MAPbI_{3-x}Cl_x$ and TiO_2 NRs (w)/$MAPbI_{3-x}Cl_x$. It demonstrated that the perovskite $MAPbI_{3-x}Cl_x$ presents a good light-harvesting capability over the visible to near-IR spectrum. The absorption intensity of TiO_2 NRs (w)/$MAPbI_{3-x}Cl_x$ is larger than that of TiO_2 NRs (e)/$MAPbI_{3-x}Cl_x$ at the 430-580 nm range could be due to the effect of TiO_2 NRs (Figure 6B, inset). The absorption difference between TiO_2 NRs (e) and TiO_2 NRs (w) could be due to the different properties, such as orientation, length, diameter, and density. Compared with TiO_2 NRs (e), TiO_2 NRs (w) appear a loosely aligned array as shown in Figure 5. Specially, for a loosely aligned array, the incident light can be multi-reflected between nanorods, promoting the absorption intensity of the film [25].

To get some information on the charge dissociation and recombination processes, stead-state photoluminescence (PL) and time-resolved photoluminescence (TRPL) were performed. Figure 7A shows the normalized PL spectra of FTO/$MAPbI_{3-x}Cl_x$, FTO/TiO_2 NRs (e)/$MAPbI_{3-x}Cl_x$, and FTO/TiO_2 NRs (w)/$MAPbI_{3-x}Cl_x$. The photoluminescence peak at 780 nm is consistent with previous report of emission from $MAPbI_{3-x}Cl_x$ [27]. From the PL intensity, there is a substantial quenching effect when the perovskite layer contacts with TiO_2 nanorods films. The PL quenching with the TiO_2 NRs (w) is more dramatic than that with TiO_2 NRs (e), which indicates that TiO_2 NRs (w) is more effective than TiO_2 NRs (e) for electron extraction. Figure 7B shows the TRPL of spectra of FTO/$MAPbI_{3-x}Cl_x$, FTO/TiO_2 NRs (e)/$MAPbI_{3-x}Cl_x$, and FTO/TiO_2 NRs (w)/$MAPbI_{3-x}Cl_x$. The TRPL curve was fitted to a biexponential function (Eq.1),

$$I(t) = A_1 \exp(\frac{t}{\tau_1}) A_2 + \exp(\frac{t}{\tau_2}) \qquad (1)$$

The detailed parameters are summarized in Table 1. The fast decay (τ_1) could be originated from the transportation of free carriers from perovskite layer to the respective hole or electron contact. The slow decay (τ_2) could be attributed to the radiative recombination of free charge carriers before the charge collection [28-30]. For the sample of FTO/$MAPbI_{3-x}Cl_x$, the slow decay time is 188.90 ns, which agrees

with that reported in the literature [27, 31]. For the sample of FTO/TiO_2 NRs (e)/ $MAPbI_{3-x}Cl_x$, the fast decay time is 40.03 ns with a fraction of 32.23%, and the slow decay time is 111.30 ns with a fraction of 67.77%. In contrast, for the sample of FTO/TiO_2 NRs (w)/$MAPbI_{3-x}Cl_x$, the fast decay time (28.47 ns) and slow decay time (103.50 ns) was both shortened, and the fraction of fast decay process (41.20%) was increased. This indicates that the charge transfer from perovskite layer to TiO_2 nanorods film for TiO_2 NRs (w)/$MAPbI_{3-x}Cl_x$ junction is faster than that for TiO_2 NRs (e)/$MAPbI_{3-x}Cl_x$ junction, and the charge recombination of TiO_2 NRs (w)/$MAPbI_{3-x}Cl_x$ is more reduced than that of TiO_2 NRs (e)/$MAPbI_{3-x}Cl_x$.

Based on the IPCE theory, IPCE=$\eta_{lh}\times\eta_{e\text{-}inj}\times\eta_{h\text{-}inj}\times\eta_{cc}$, where η_{lh} is light harvesting efficiency, $\eta_{e\text{-}inj}$ is electron injection efficiency, $\eta_{h\text{-}inj}$ is hole injection efficiency, and η_{cc} is charge collection efficiency. $\eta_{h\text{-}inj}$ and η_{cc} are considered to be similar because the HTM layer and metal electrodes are identical. The UV-vis absorption indicates that η_{lh} of the cells based on TiO_2 NRs (w) is larger than that on TiO_2 NRs (e). The PL and TRPL suggest that $\eta_{e\text{-}inj}$ of the cells based on TiO_2 NRs (w) is higher than that on TiO_2 NRs (e). Therefore the higher photovoltaic performance of TiO_2 NRs (w) based cells is due to its larger light harvesting efficiency and electron injection efficiency.

Electrochemical impedance spectroscopy (EIS) is a powerful technique to evaluate the charge transfer behavior in solar cells [32]. The EIS of FTO/TiO_2 NRs/$MAPbI_{3-x}Cl_x$/spiro-MeOTAD/Au solar cells were performed. Figure 8A shows the Nyquist plots of the cells based on TiO_2 NRs (e) and TiO_2 NRs (w), in which two RC arcs were observed. The data were fitted to a simple equivalent circuit shown in Figure 8B. The high-frequency RC element is attributed to the contact resistance (R_{co}) at the interfaces, while the low-frequency element is ascribed to the recombination resistance (R_{rec}) and chemical capacitance (C_μ) of the system, and R_s is an additional contribution from series resistance [19, 33]. The values of fitting parameters are listed in Table 2. The contact resistance (R_{co}) and total series resistance (R_s+R_{co}) for the cells based on TiO_2 NRs (w) are smaller than those on TiO_2 NRs (e), while the recombination resistance (R_{rec}) on TiO_2 NRs (w) is larger than that on TiO_2 NRs (e), which indicates that an enhanced charge transport ability and induced carrier

recombination rate for the cells based on TiO_2 NRs (w). This agrees well with the J-V measurements.

The stability of solar cells is an important parameter for their applications. Therefore the air stability of the cells based on TiO_2 NRs was investigated. Figure 9 shows the air stability as a function of storage time under ambient conditions without encapsulation. Both the solar cells based on TiO_2 NRs (e) and TiO_2 NRs (w) degraded gradually under these conditions. While the average degradation rate of TiO_2 NRs (w) based cells was slower than that of TiO_2 NRs (e) based cells.

By optimizing the parameters, we achieved the PCE as high as 11.8% for the $MAPbI_{3-x}Cl_x$ perovskite solar cells based on the TiO_2 NRs (w). In the reported perovskite solar cells based on TiO_2 NRs, the highest PCE of the cells is 11.1% [34]. The $CH_3NH_3PbI_3$ was usually adopted as an active layer in most of the TiO_2 NRs based perovskite solar cells [18-20], while the $MAPbI_{3-x}Cl_x$ was choose as the absorber layer in the present study. The energy band diagrams of TiO_2, $CH_3NH_3PbI_3$, $MAPbI_{3-x}Cl_x$, and Spiro-OMeTAD are shown in Figure 10 according to the literatures [1, 35]. The conduction band of $MAPbI_{3-x}Cl_x$ is located at -3.75 eV relative to absolute vacuum scale (AVS), which is higher than that of $CH_3NH_3PbI_3$ (-3.93 eV vs AVS). The conduction band difference between $MAPbI_{3-x}Cl_x$ and TiO_2 is larger than that between $CH_3NH_3PbI_3$ and TiO_2, which is more beneficial for the electron injection from perovskite material to the ETM layer [36, 37]. Therefore the high PCE of the TiO_2 NRs (w) based $MAPbI_{3-x}Cl_x$ perovskite solar cells in this study could be due to the large conduction band difference between $MAPbI_{3-x}Cl_x$ and TiO_2 NRs (w).

Conclusion

In summary, TiO_2 NRs (e) and TiO_2 NRs (w) were synthesized by the hydrothermal methods with ethanol-HCl and water-HCl solutions, respectively. $MAPbI_{3-x}Cl_x$ perovskite solar cells were fabricated using the TiO_2 NRs as an ETM. The performance of the solar cells was optimized by changing the growth time of TiO_2 NRs. The PCEs of the best solar cells based on TiO_2 NRs (w) is higher than that on TiO_2 NRs (e). To explain this phenomenon, some investigations were performed.

SEM images displays that TiO_2 NRs (w) appears a higher degree of order and alignment than TiO_2 NRs (e), and the thickness of perovskite capping layer in the cells based on TiO_2 NRs (w) is more uniform than that on TiO_2 NRs (e). UV-vis absorption spectra display TiO_2 NRs (w) has a better optical propriety than TiO_2 NRs (e). PL, TRPL, and EIS spectra indicate that the charge transfer for TiO_2 NRs (w) is faster than for TiO_2 NRs (e), while the charge recombination for TiO_2 NRs (w) is more reduced than for TiO_2 NRs (e). The PCE as high as 11.8% was achieved for the $MAPbI_{3-x}Cl_x$ perovskite solar cells based on TiO_2 NRs (w) by optimizing the parameters of TiO_2 NRs.

Experimental

Materials Preparation

Methylammonium iodide (CH_3NH_3I) was synthesized using a previously reported method [26]. Typically, aqueous solution of hydroiodic acid (HI) (5 mL, 57 wt% in water, Aladdin Reagent) was reacted with methylamine (CH_3NH_2) (12 mL, 33 wt% in absolute ethanol, Aladdin reagent) at 0°C for 2 h with constant stirring under nitrogen atmosphere. Methylammonium was crystalized by removing the solvent with a rotary evaporator. The generated white powder was washed with diethyl ether for three times and dried in vacuum for overnight at 60°C. The perovskite precursor solution was prepared by dissolving CH_3NH_3I and lead (II) chloride ($PbCl_2$) in anhydrous *N*,*N*-Dimethylformamide (DMF) at a 3:1 molar ratio at 60°C.

FTO-coated glass substrate (~15 ohm/sq, NPG, Japan) was patterned by etching with Zn metal powder and 2M HCl diluted in deionized water, and cleaned by sonication for 15 min in detergent, acetone, 2-propanol, and ethanol, respectively. Oxygen plasma was subsequently used to treat the substrate for 20 min. A compact layer of TiO_2 was formed on FTO by treating the substrate in an 0.2 M aqueous solution of $TiCl_4$ at 70°C for 30 min. TiO_2 nanorods were grown on the compact layer by ethanol–HCl and water–HCl hydrothermal methods previously reported [22, 19]. In brief, 20 mL of 37% hydrochloric acid and 20 mL of ethanol or 20 mL of deionized water were mixed. Subsequently 0.7 mL of titanium(IV) n-butoxide (99%, Aladdin

reagent) was added. After stirring for 30 min, the mixed solution and a compact layer coated FTO substrate was sealed in a stainless steel autoclave with Teflon liner of 50 mL capacity. The sealed autoclave was placed inside the oven preheated to 170°C for several hours. After cooling down to room temperature, the TiO_2 nanorod film was rinsed with ethanol and deionized water, and annealed at 500℃ for 60 min. The TiO_2 nanorods samples prepared with ethanol–HCl and water–HCl hydrothermal methods were nominated as TiO_2 NRs (e) and TiO_2 NRs (w), respectively.

Solar Cell fabrication

The perovskite precursor solution was spin-coated on the annealed TiO_2 nanorod film at 2000 rpm for 60 s in an argon-filled glove box. The sample was dried on a hotplate at 110°C for 60 min. The hole-transporter layer was deposited by spincoating a spiro-OMeTAD solution at 1500 rpm for 60 s. The spiro-MeOTAD solution was prepared by dissolving 72.3 mg of spiro-MeOTAD in 1 ml of chlorobenzene, to which 28.8 μl of 4-tert-butylpyridine and 17.5 μl of lithiumbis(trifluoromethanesulfonyl)imide(Li-TFSI) solution (520 mg LI-TSFI in 1 ml acetonitrile, Aladdin reagent) were added. Finally, a thin gold layer was thermally evaporated on top of the device.

Characterization

X-ray diffraction (XRD) patterns were recorded on a DX-2700 diffractometer with Cu Kα radiation with λ =0.1542 nm. Photocurrent-voltage (*J-V*) measurements were performed using a Keithley 2440 Sourcemeter under AM 1.5 G illumination from a Newport Oriel Solar Simulator with an intensity of 100 mW/cm^2. The active area was 0.1 cm^2 determined by a shadow mask. The J-V curves were obtained in the air with a step size of 20 mV and sampling delay time of 1000 ms. Incident photon to current conversion efficiency (IPCE) was determined using Qtest Station 500ADX (America). Morphologies and microstructures were observed with a scanning electron

microscope (SEM, JEM-7001F, JEOL). UV-vis absorption spectra were collected on a UV–vis spectrophotometer (Varian Cary 5000). Steady-state photoluminescence (PL) and time-resolved photoluminescence (TRPL) measurements were acquired with a FLS 980 E fluorometer (Edinburgh Photonics), using a pulsed diode laser as an excitation source. The electrochemical impedance measurements were performed under a forward bias of 0.6 V under 1 sun illumination conditions with an electrochemical workstation (CHI660e, Shanghai CHI Co., Ltd.) with the frequency range from 1 Hz to 300 kHz. The magnitude of the alternative signal was 10 mV.

Acknowledgements

This work is supported by the Science and Technology Development Project of Henan Province (No.142300410157 and No.142102210389), National Natural Science Foundation of China (No. 21103043), Scientific Research Foundation for the Returned Overseas Chinese Scholars, State Education Ministry, and Program for Innovative Research Team (in Science and Technology) in University of Henan Province (No. 13IRTSTHN017).

Reference

1 H. Kim, C. Lee, J. Im, K. Lee, T. Moehl, A. Marchioro, S. Moon, R. Humphry-Baker, J. Yum, J. Moser, M. Gratzel and N. Park, *Sci. Rep.*, 2012, **2**, 591.

2 W. Nie, H. Tsai, R. Asadpour, J. C. Blancon, A. J. Neukirch, G. Gupta, J. J. Crochet, M. Chhowalla, S. Tretiak and M. A. Alam, *Science*, 2015, **347**, 522.

3 Q. Dong, Y. Fang, Y. Shao, P, Mulligan, J. Qiu, L. Cao and J. Huang, *Science*, 2015, **347**, 967.

4 G. Xing, N. Mathews, S. Sun, S. S. Lim, Y. M. Lam, M. Graetzel, S. Mhaisalkar

and T. C. Sum, *Science*, 2013, **342**, 344.

5 M. Liu, M. B. Johnston and H. J. Snaith, *Nature*, 2013, **501**, 395.

6 J. Burschka, N. Pellet, S. J. Moon, R. H. Baker, P, Gao, M. K. Nazeeruddin and M. Gratzel, *Nature*, 2013, **499**, 316.

7 A. Y. Mei, X. Li, L. F. Liu, Z. L. Ku, T. F. Liu, Y. G. Rong, M. Xu, M. Hu, J. Z. Chen, Y. Yang, M. Gratzel and H. W. Han, *Science*, 2014, **345**, 295.

8 N. J. Jeon, J. H. Noh, W. S. Yang, Y. C. Kim, S. C. Ryu, J. W. Seo and S. I. Seok, *Nature*, 2015, **517**, 476.

9 H. Zhou, Q. Chen, G. Li, S. Luo, T. B. Song, H. S. Duan, Z. Hong, J. You, Y. Liu and Y. Yang, *Science,* 2014, **345**, 542.

10 W. S. Yang, J. H. Noh, N. J. Jeon, Y. C. Kim, S. Ryu, J. Seo and S. I. Seok, *Science*, 2015, **348**, 1234.

11 J. H. Heo, S. H. Im, J. H. Noh, T. N. Mandal, C.S. Lim, J. A. Chang, Y. H. Lee, H. J. Kim, A. Sarkar, M. K. Nazeeruddin, M. Gratzel and S. I. Seok, *Nat. Photonics*, 2013, **7**, 487.

12 K. Mahmood, B. S. Swain, A. R. Kirmani, A. Amassian, *J. Mater. Chem. A*, 2015, **17**, 9051.

13 B. Cai, Y. Xing, Z. Yang, W. H. Zhang and J. Qiu, *Energy Environ. Sci.*, 2013, **6**, 1480.

14 N. J. Jeon, J. H. Noh, Y. C. Kim, W. S. Yang, S. I. Seok, *Nat. Mater.*, 2014, **13**, 897.

15 H. J. Snaith, R. Humphry-Baker, P. Chen, I. Cesar, S. M. Zakeeruddin and M. Gratzel, *Nanotechnology*, 2008, **19**, 424003.

16 S. H. Kang, S. H. Choi, M. S. Kang, J. Y. Kim and H. S. Kim, *Adv. Mater.*, 2008, **20**, 54.

17 D. Y. Son, K. H. Bae, H. S. Kim and N. G. Park, *J. Phys. Chem. C*, 2015, **119**, 10321.

18 J. Qiu, Y. Qiu, K. Yan, M. Zhong, C. Mu, H. Yan and S. Yang, *Nanoscale*, 2013, **5**, 3245.

19 H. S. Kim, J. W. Lee, N. Yantara, P. P. Boix, S. A. Kulkarni, S. Mhaisalkar, M.

Gratzel and N. G. Park, *Nano Lett.*, 2013, **13**, 2412.

20 D. Zhong, B. Cai, X. L. Wang, Z. Yang, Y. D. Xing, S. Miao, W. H. Zhang and C. Li, *Nano Energy*, 2015, **11**, 409.

21 D. Y. Son, J. H. Im, H. S. Kim and N. G. Park, *J. Phys. Chem. C*, 2014, **118**, 16567.

22 Y. Zhang, W. Q. Liu, F. R. Tan and Y. Z. Gu, J. Power Sources, 2015, **74**, 1224.

23 S. Ito, S. M. Zakeeruddin, R. H. Baker, P. Liska, R. Chavet, P. Comte, M. K. Nazeeruddin, P. Pechy, M. Takata, H. Miura, S. Uchida and M. Gratzel, *Adv. Mater.*, 2006, **18**, 1202.

24 F. Zhang and X. H. Liu, *Thin Solid Films*, 1998, **326**, 171.

25 X. X. Wang, Y. D. Xiao, D. W. Zeng and C. S. Xie, *CrystEngComm*, 2015, **17**, 1151.

26 M. M. Lee, J. Teuscher, T. Miyasaka, T. N. Murakami and H. J. Snaith, *Science*, 2012, **338**, 643.

27 S. D. Stranks, G. E. Eperon, G. Grancini, C. Menelaou, M. J. P. Alcocer, T. Leijtens, M. Laura, M. Herz, A. Petrozza and H. J. Snaith, *Science*, 2013, **342**, 341.

28 P. W. Liang, C. Y. Liao, C. C. Chueh, F. Zuo, S. T. Williams, X. K. Xin, J. Lin and A. K. Y. Jen, *Adv.Mater.*, 2014, **26**, 3748.

29 Q. Chen, H. Zhou, T. B. Song, S. Luo, Z. Hong, H. S. Duan, L. Dou, Y. Liu and Y. Yang, *Nano Lett.*, 2014, **14**, 4158.

30 J. S. Yeo, R. Kang, S. Y. Lee, Y. J. Jeon, N. S. Myoung, C. L. Lee, D. U. Kim, J. M. Yun, Y. H. Seo, S. S. Kim and S. I. Na, *Nano Energy*, 2015, **12**, 96.

31 S. Bai, Z. W. Wu, X. J. Wu, Y. Z. Jin, N. Zhao, Z. H. Chen, Q. Q. Mei, X. Wang, Z. Z. Ye, T. Song, R. Y. Liu, S. T. Lee and B. Q. Sun, *Nano Research*, 2014, **7**, 1749.

32 H. S. Kim, I. Mora-Sero, V. Gonzalez-Pedro, F. Fabregat-Santiago, E. J. Juarez-Perez, N. G. Park, J. Bisquert, *J. Nat. Commun.*, 2013, **4**, 2242.

33D. Y. Liu, J. L. Yang and T. L. Kelly, *J. Am. Chem. Soc.*, 2014, **136**, 17116.

34 B. Cai, D. Zhong, Z. Yang, B. K. Huang, S. Miao, W. H. Zhang, J. S. Qiu and C.

Li, *J. Mater. Chem. C*, 2015, **3**, 729.

35 A. Abrusci, S. D. Stranks, P. Docampo, H. L. Yip, A. K. Y. Jen and H. J. Snaith, *Nano Lett.*, 2013, **13**, 3124.

36 K. Tvrdy, P. Frantszov and P. V. Kamat, *Proc. Nat. Acad. Sci. U. S.*, 2011, **108**, 29.

37 I. Robel, M. Kuno and P. V. Kamat, *J. Am. Chem. Soc.*, 2007, **129**, 4136.

Figure Captions

Figure 1 XRD patterns of TiO_2 NRs (e) and TiO_2 NRs (w).

Figure 2 Dependence of power conversion efficiency (PCE) of solar cells on the growth time.

Figure 3 J-V curves of the best solar cells based on TiO_2 NRs (e) and TiO_2 NRs (w).

Figure 4 IPCE spectra with integrated current densities of the perovskite solar cells based on TiO_2 NRs (e) and TiO_2 NRs (w).

Figure 5 Plane-view and cross sectional SEM images. (a) and (c) TiO_2 NRs (e) films for 60 min growth, (b) and (d) TiO_2 NRs (w) films for 120 min growth. Cross sectional SEM images of the best solar cells based on (e) TiO_2 NRs (e), and (f) TiO_2 NRs (w).

Figure 6 (A) XRD patterns of TiO_2 NRs/$MAPbI_{3-x}Cl_x$. (B) UV-vis absorption spectra of TiO_2 NRs/$MAPbI_{3-x}Cl_x$. The inset shows the UV-vis absorption spectra of TiO_2 NRs.

Figure 7 (A) Stead-state photoluminescence spectra. (a) FTO/$MAPbI_{3-x}Cl_x$, (b) FTO/TiO_2 NRs (e)/$MAPbI_{3-x}Cl_x$, (c) FTO/TiO_2 NRs (w)/$MAPbI_{3-x}Cl_x$. (B) Time-resolved photoluminescence spectra. (a) FTO/$MAPbI_{3-x}Cl_x$, (b) FTO/TiO_2 NRs (e)/ $MAPbI_{3-x}Cl_x$, (c) FTO/TiO_2 NRs (w)/$MAPbI_{3-x}Cl_x$.

Figure 8 (A)Typical Nyquist plots for the perovskite solar cells based on TiO_2 NRs, as measured under 1 sun illumination. The simulation result (solid line) is fitted to experimental data (symbols). (B) Equivalent circuit applied to fit the Nyquist plots.

Figure 9 Normalized PCE as a function of storage time for the cells based on TiO_2 NRs exposed to ambient air without encapsulation.

Figure 10 Energy band diagrams of TiO_2, $CH_3NH_3PbI_3$, $MAPbI_{3-x}Cl_x$, and Spiro-OMeTAD.

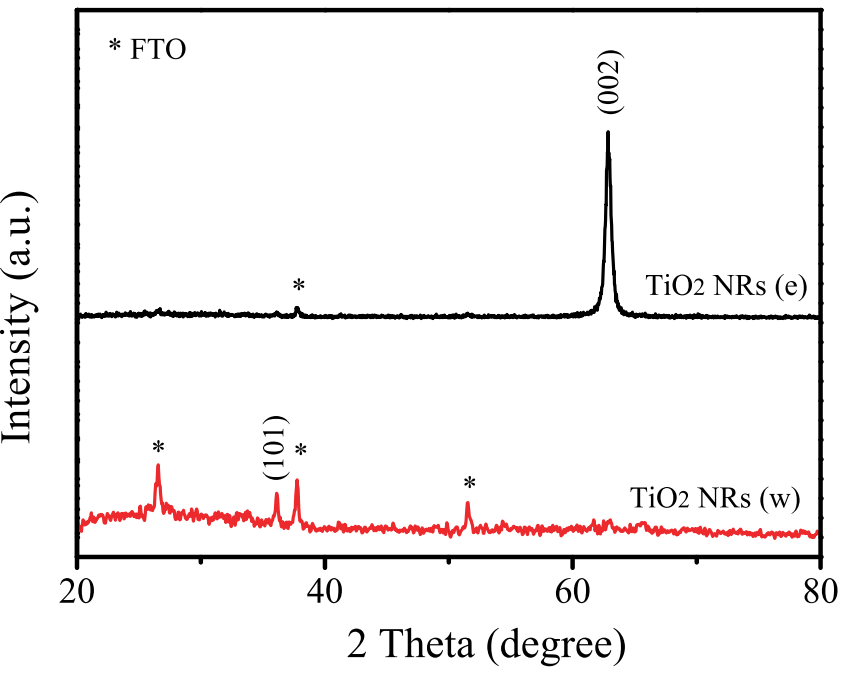

Figure 1

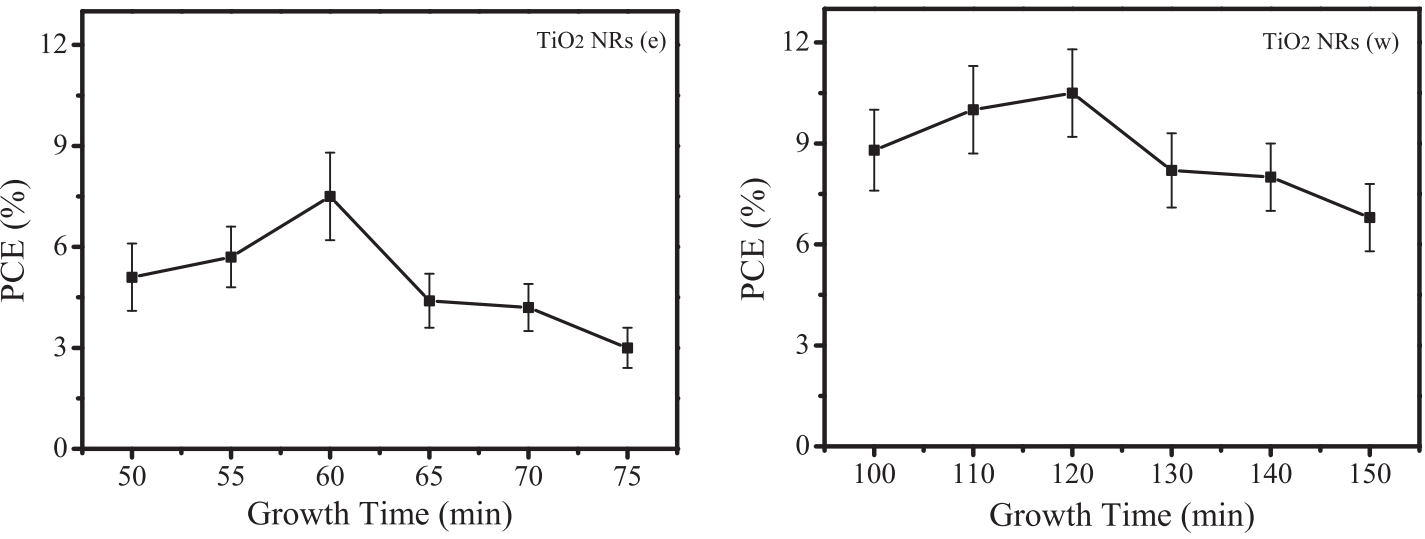

Figure 2

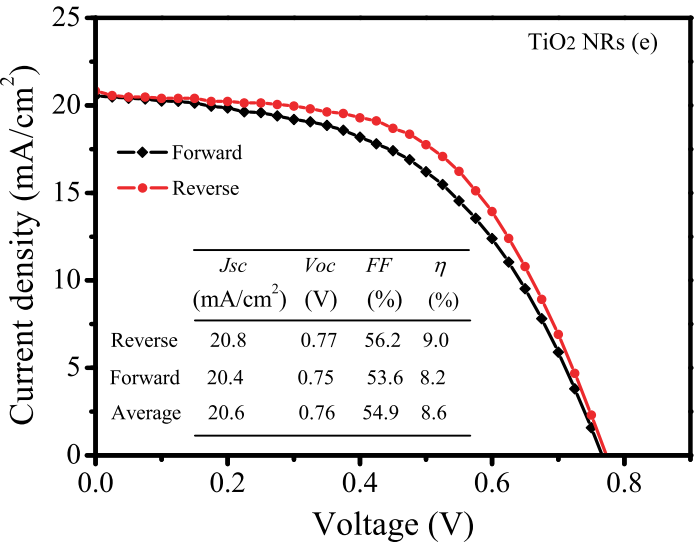

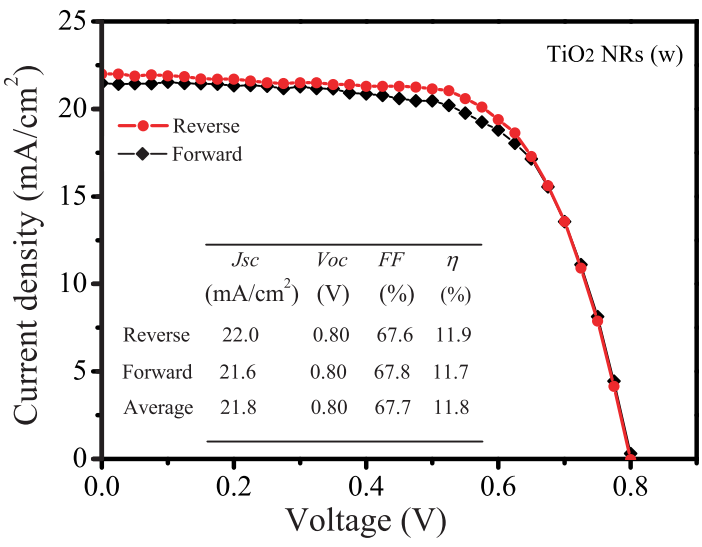

Figure 3

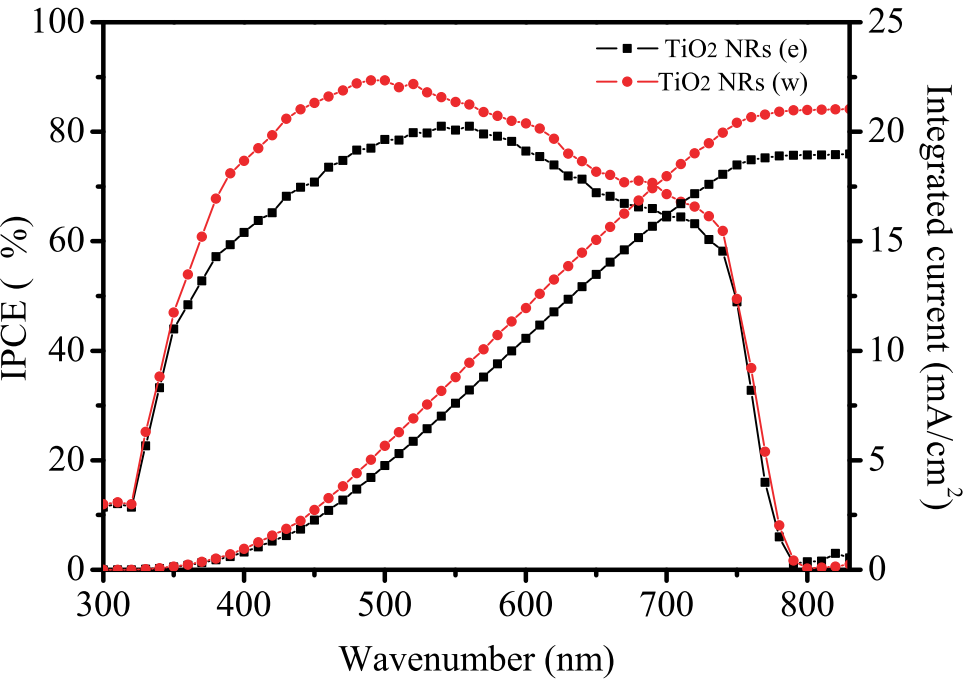

Figure 4

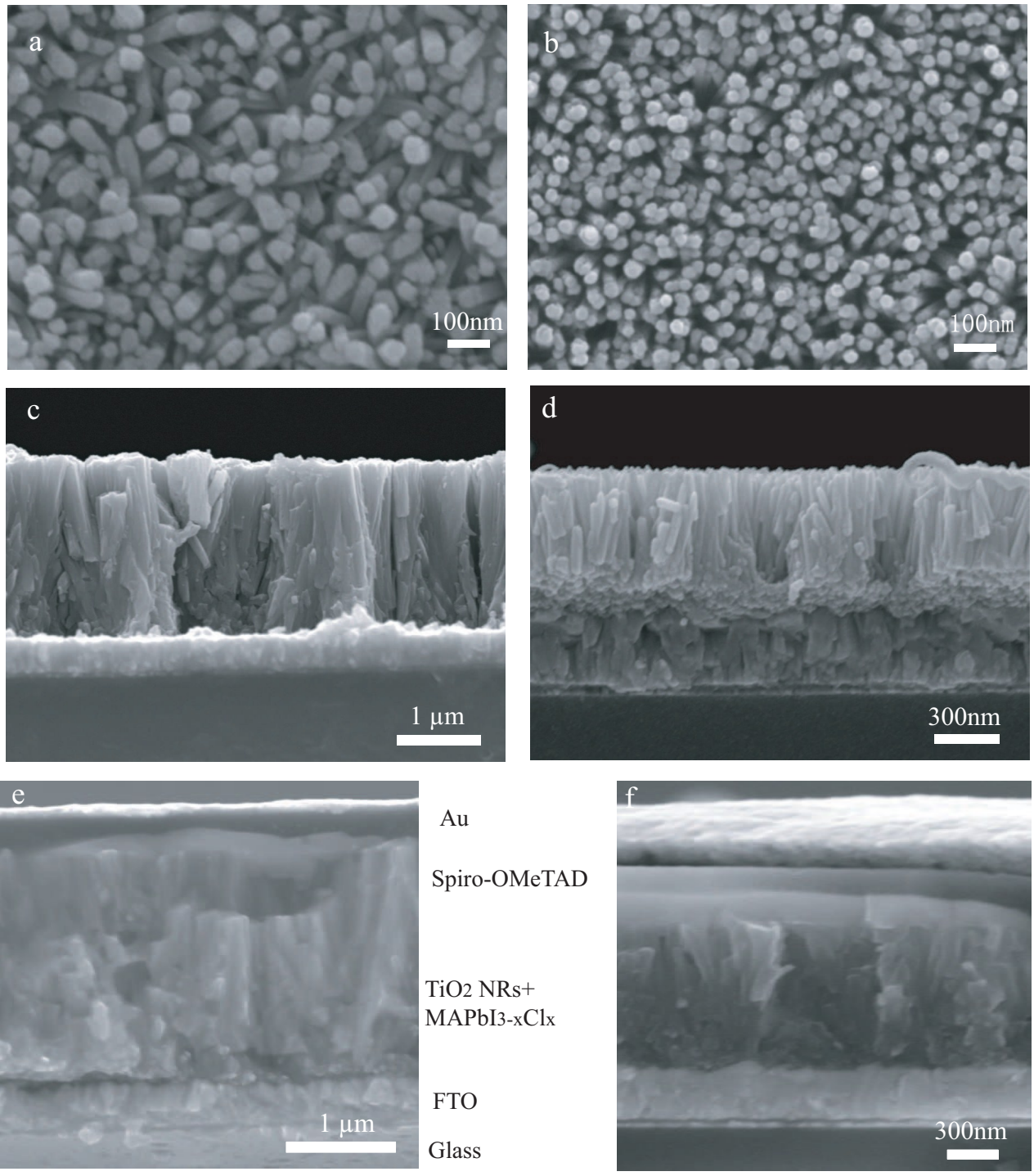

Figure 5

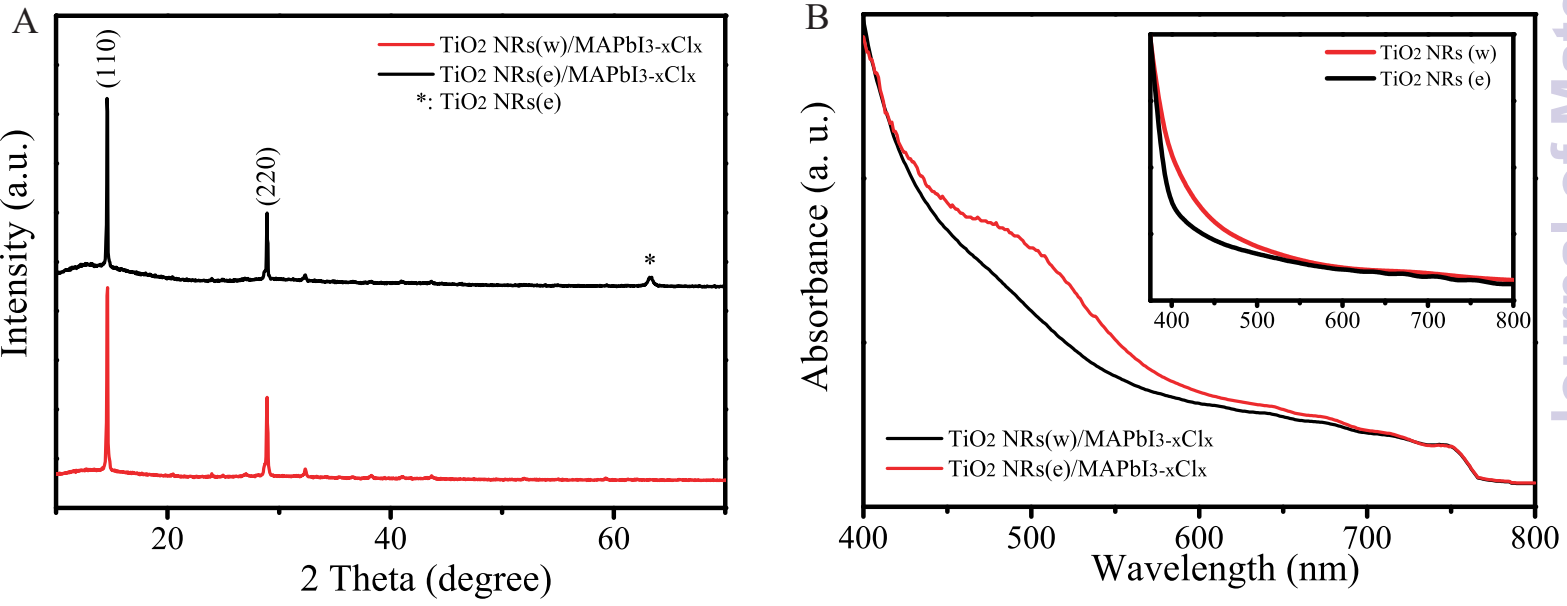

Figure 6

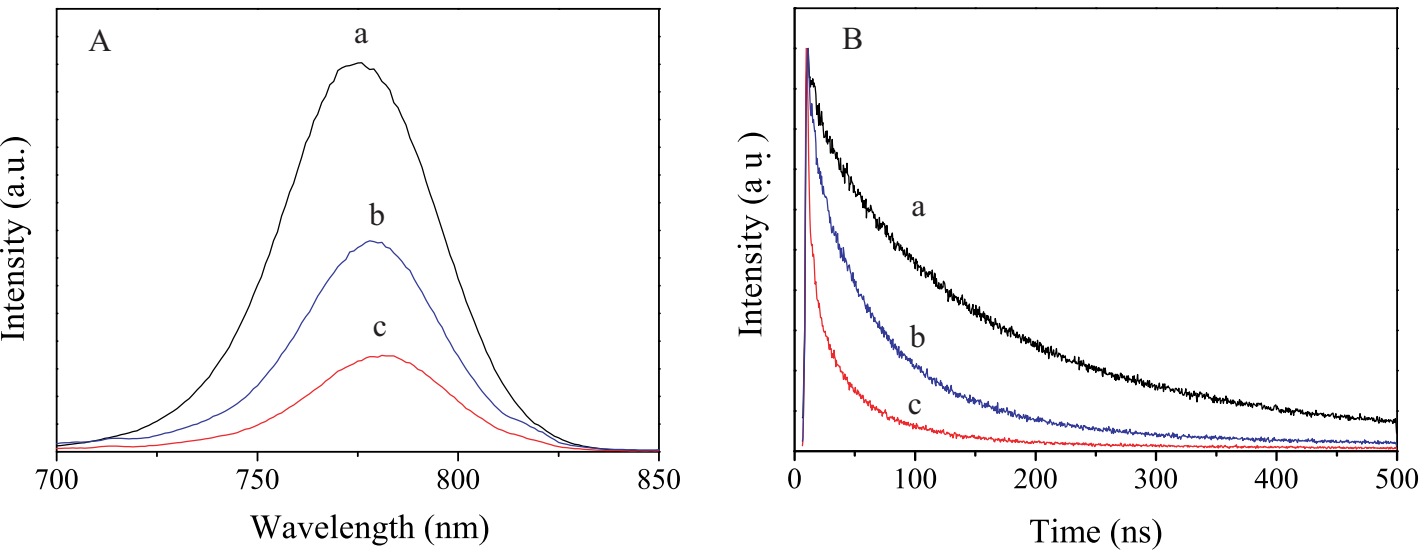

Figure 7

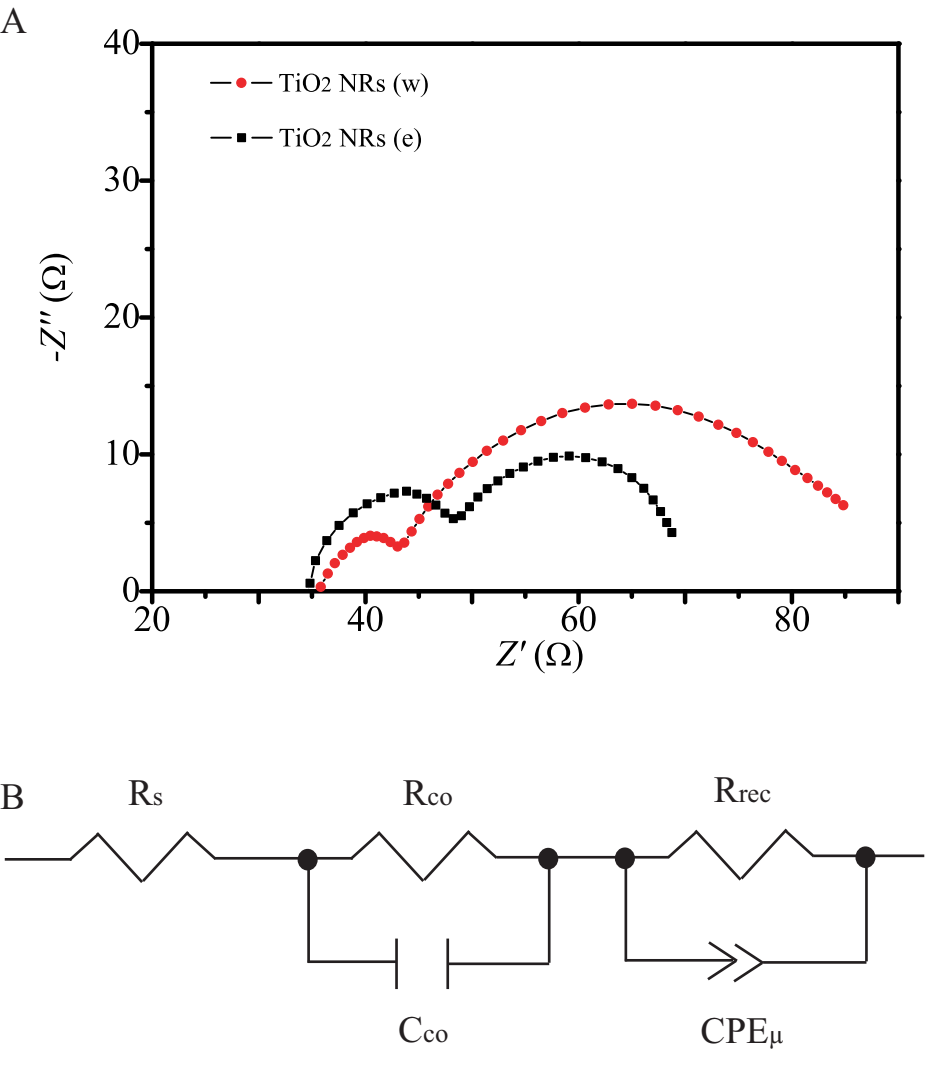

Figure 8

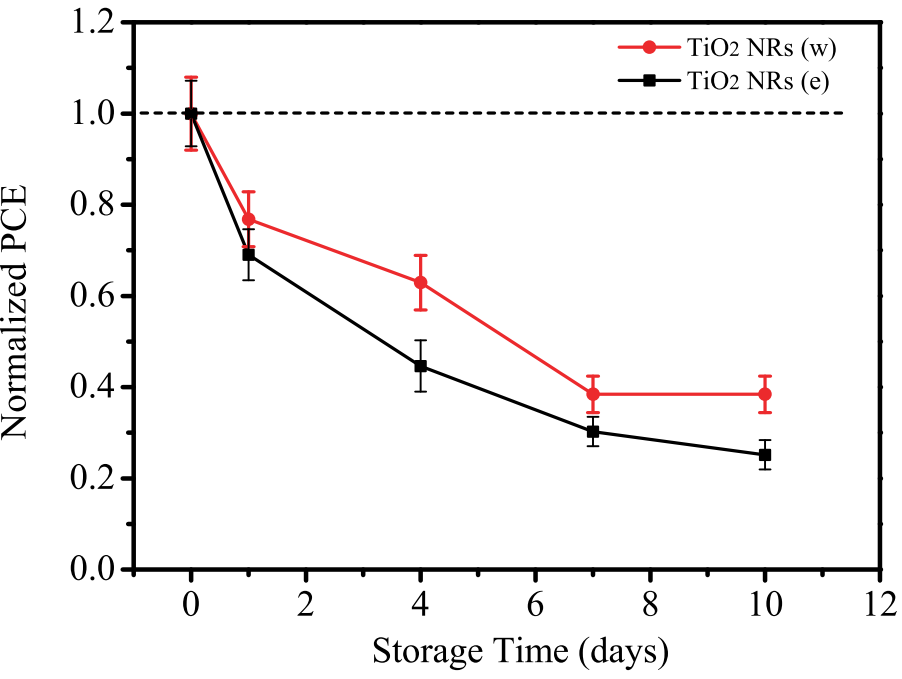

Figure 9

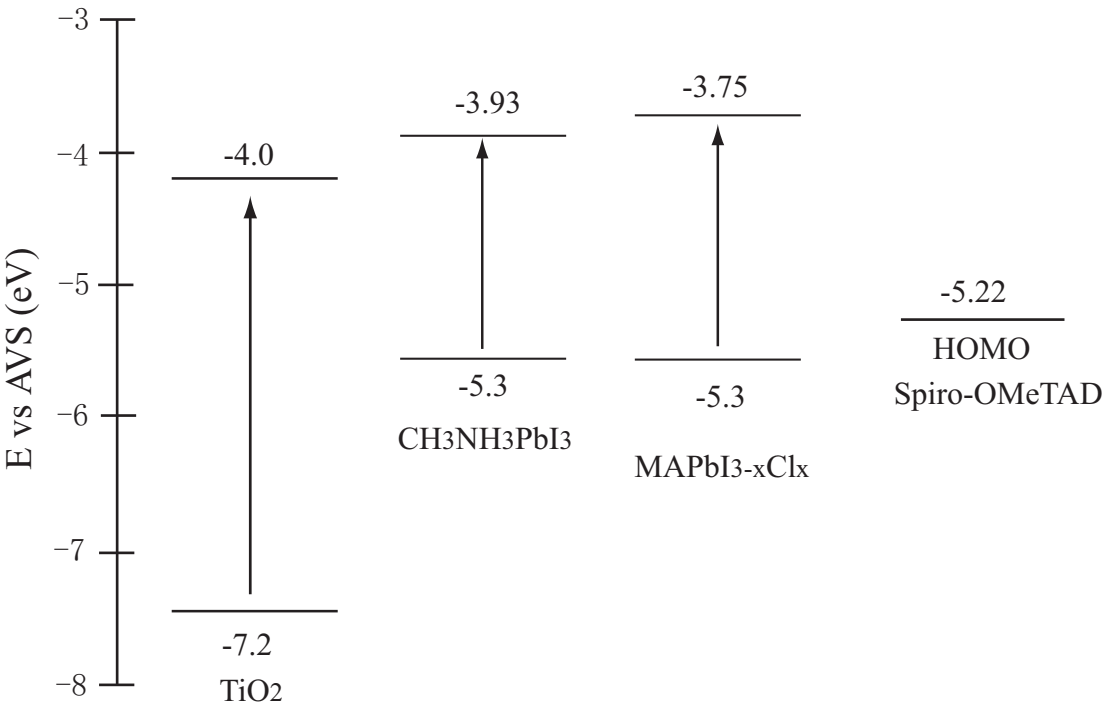

Figure 10

Table 1 Parameters of the TRPL spectra

Samples	τ_1/ns	% of τ_1	τ_2/ns	% of τ_2
FTO/$CH_3NH_3PbI_{3-x}Cl_x$	65.28	10.67	188.90	89.33
FTO/TiO_2 NRs (e)/$CH_3NH_3PbI_{3-x}Cl_x$	40.03	32.23	111.30	67.77
FTO/TiO_2 NRs (w)/$CH_3NH_3PbI_{3-x}Cl_x$	28.47	41.20	103.50	58.80

Table 2 Fitting parameters for EIS data.

TiO_2 NRs based cell	R_s/Ω	R_{co}/Ω	R_{rec}/Ω	C_{co}/Ω	CPE-T/F	CPE_μ-P
TiO_2 NRs (e)	35.6	14.6	26.9	7.3E-8	6.7E-6	0.79
TiO_2 NRs(w)	36.5	8.6	44.9	1.6E-7	1.7E-5	0.73

Graphical Abstract

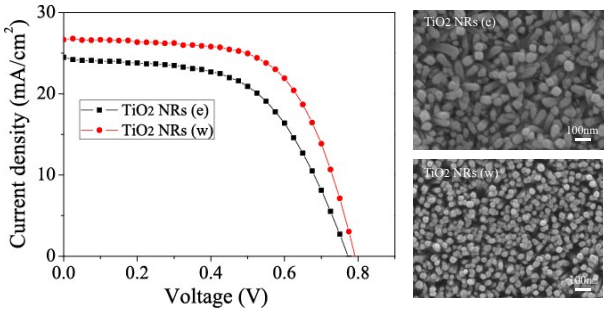

The PCE of cells based on TiO_2 NRs (w) (11.8%) is higher than that on TiO_2 NRs (e) (8.6%), which is the highest in the reported TiO_2 NRs based cells.